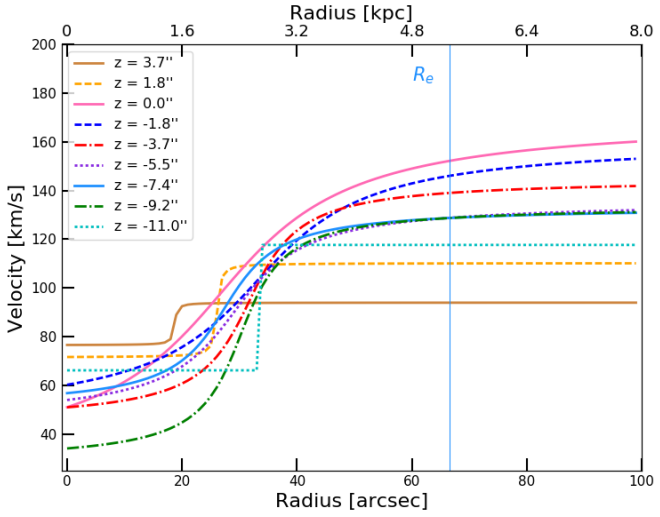

Fig. 10. Envelopes corrected from the morphological inclination (89.5°) of the different PVDs shown in Fig. 8. The vertical blue dotted line indicates the effective radius $R_e(i)$.

Levy et al. 2019) and radio (e.g., Miller & Veilleux 2003; Fraternali & Binney 2006; Zschaechner & Rand 2015) wavelengths, including in the Milky Way (e.g., Kalberla et al. 2014). This phenomenon has been explained by a combination of vertical movements due to energy input from galactic fountains, radial movements of the gas due to the pressure gradient of the halo and a declining rotation velocity due to the conservation of the angular momentum (Fraternali & Binney 2006; Heald et al. 2007). This vertical velocity gradient can be modified whenever a galaxy such as NGC 4330 is suffering an external perturbation. In NGC 4330, the amplitude of the RC does not decrease sufficiently with the vertical distance from the disc plane to explain the observed lags. In this galaxy, which is suffering an almost face-on ram pressure stripping event, galactic fountains were probably suppressed, in particular in the upwind side of the disc where the external pressure is significantly increased.

The lag gradient of NGC 4330 can be estimated by measuring the change in velocity along the z axis using the PVDs parallel to the major axis. Once corrected from the morphological inclination of the galaxy (89.5°), the envelopes of the different PVDs shown in Fig. 8 become the RCs given in Fig. 10. The RC with the highest velocity amplitude is obtained in the plane of the disc ($z = 0$ arcsec). To the south-west, at the effective radius, the velocity decreases by $\langle \Delta V \rangle \simeq 9$ km s^{-1} each $\Delta z = 1.8$ arcsec (~0.14 kpc) from the kinematic major axis up to $z = -5.5$ arcsec (~0.4 kpc), where, because the ram pressure stripping compresses the gas, there is no change in velocity along the z axis up to -11 arcsec (~0.9 kpc), where the most diffuse gas is. To derive the velocity gradient along the z axis of NGC 4330 we used the fact that the asymptotic velocity V_0 of the relation (B.4) is one of the free parameters of the fitting to the terminal velocity of each PVD, so that, from $z = 0$ to -5.5 arcsec (~0.4 kpc) there is a lag gradient of $\Delta V/\Delta z \sim 64 \pm 9$ km s^{-1} kpc^{-1}. The rotation in the north along the z axis has been modified by the wind, it is slower by $\Delta V = 49$ km s^{-1} with respect to the one measured at $z = 0$ arcsec. The difference in velocity between the northern RCs is $\Delta V = 16$ km s^{-1}. Although the rotation velocity decreases with the distance from the stellar disc, as indeed expected, it is not possible to determine a constant lag gradient in this direction.

6.3. PVDs along the minor axis

The ram pressure stripping event, which is acting almost face-on in NGC 4330, has reduced the vertical height of the ionised gas disc in the northern direction (upwind). We thus study the PVDs along the kinematic minor axis to determine whether galactic fountains or inflows have been suppressed by the external pressure (e.g., Heald et al. 2006, 2007; Rosado et al. 2013). Figure 9 shows the PVDs perpendicular to the kinematic major axis obtained from the PUMA dataset. The pseudo-slits are located in specific places to highlight the main features of the disc and its asymmetries, and they cross the regions labelled from A to M identified in Sect. 2. We also compare the PVDs from the observational data with the PVDs at the same position obtained from that data cube model computed with the ITM (see Sect. 4).

In general, these PVDs show that the brightest Hα emitting gas is compressed to the galactic mid plane and that it follows mostly the rotation predicted by the cylindrical model. Upwind (north-east) there is no Hα emitting gas beyond $z \simeq 5$ arcsec (0.4 kpc). Only near the midplane of the disc, downwind (south-west) the gas decreases its brightness along the $z-$axis following the exponential structure used to construct the model. Here the velocity of the most diffuse gas generally increases with z all over the galactic disc. This increase in velocity with z is not reproduced by the ITM model.

In region A, at 65.5 arcsec (5.2 kpc) from the kinematic centre, the ionised gas has exactly the same velocity of the cylindrical model. At 31.7 arcsec (2.5 kpc), the low radial velocity observed for the gas in region D in the velocity field is now evident as long as its corresponding position on the disc follows the model. We only detected some diffuse gas to the north-east along the $z-$axis inside region F at a radius of 4.1 arcsec (0.3 kpc) from the kinematic centre, where the diffuse gas rotates a little faster than the model. The pseudo-slit at the kinematic centre shows that the gas in region E is completely compressed to the galactic mid plane. To the south-western edge of the disc, the most diffuse gas inside regions G, H, J, and K rotates slower than what expected from the model, in agreement with the residual velocity map. Finally, we have observed that the gas inside region L (-121.5 and -130.9 arcsec, 9.7 and 10.5 kpc, respectively) has a high velocity dispersion, radial and residual velocity likely because the gas is moving with non-circular motions. Figure 9 also shows that the diffuse gas in region L has a velocity higher by ~200 km s^{-1} than the one expected from the model.

Instead of a heart-shaped profile, which would indicate the presence of an inflow in the galaxy (e.g., Fraternali & Binney 2006; Rosado et al. 2013; Zschaechner et al. 2015), the PVDs suggest features similar to the intermediate- and high-velocity clouds of the Milky Way (e.g., Wakker & van Woerden 1997; Fraternali & Binney 2006) whose origin is attributed to the interaction with the Magellanic Clouds. This suggests that the kinematics of the extraplanar diffuse ionised gas of NGC 4330 is likely dominated by the ram-pressure stripping process.

7. The dynamical model

We present here the kinematical results of the simulation of NGC 4330 presented in Vollmer et al. (2021). They have been obtained using a N-body code, described in Vollmer et al. (2001), which consists of a non-collisional component plus a collisional one. The non-collisional component of 81 920 particles simulates the stellar disc, the stellar bulge and the dark halo. The collisional component simulates the ISM as an ensemble of 20 000

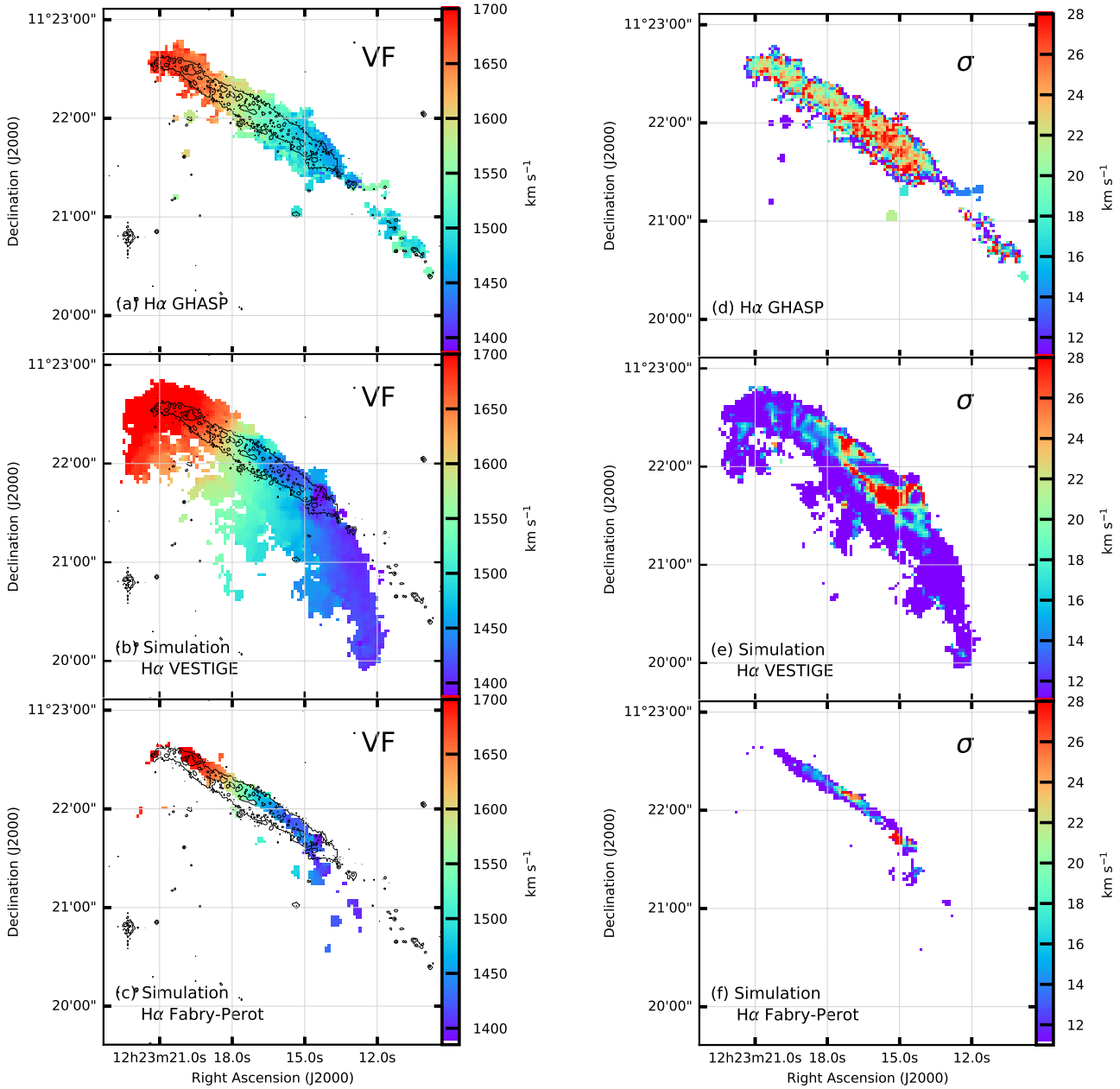

Fig. 11. GHASP (*panels a and d*) and simulated (*panels b, c, e and f*) Hα velocity (*left column*) and velocity dispersion (*right column*) fields of NGC 4330. The simulated Hα velocity and velocity dispersion fields are given down to the faintest levels used in the middle panel of Fig. C.8 to show the kinematical properties of the low column density ionised gas reached by the simulations (*panels b and e*) and at a higher surface brightness level corresponding to the sensitivity of the FP observations ($\Sigma(\mathrm{H}\alpha) \simeq 2\times10^{-17}$ erg s^{-1} cm^{-2} arcsec^{-2}, panel c). The contours on the velocity fields indicate the Hα surface brightness $\Sigma(\mathrm{H}\alpha) \sim 2\times10^{-18}$ erg s^{-1} cm^{-2} arcsec^{-2} taken from the VESTIGE data (Fossati et al. 2018).

gas clouds that have inelastic collisions (sticky particles) that might coalesce or fragment, which evolve in the gravitational potential of the galaxy. A scheme for star formation was implemented, in which stars are formed during cloud collisions to further evolve as non-collisional particles. The star formation rate is proportional to the cloud collision rate. Ram pressure has been included as an additional acceleration on the sticky particles that are not protected by other particles. Once stripped out from the galactic plane, the warm gas clouds become diffuse if their density falls below a critical density (Vollmer et al. 2021). The model consists of two components: the HII regions ionised by young massive stars with ages less than 20 Myr and the diffuse gas ionised by the stellar UV radiation or by strong shocks induced by the ram pressure stripping process. As discussed in Vollmer et al. (2021), collisional ionisation through the thermal electrons of the ambient ICM that confines the filaments is the most probable ionisation mechanism in the extraplanar ionised gas filaments detected in the VESTIGE narrow-band image.

In Figs. C.8 and 11, we compare the observed Hα data to the simulated ones. For each figure we provide three panels, the top one corresponds to the data whereas the middle and bottom ones to the models. Figures 11 (panels b and e) and C.8 (panel b) give the lowest surface brightness achieved by the model while Figs. 11 (panels c and f) and C.8 (panel c) show the model at a depth comparable to the sensitivity of our observations. The plotted Hα emission map is the one extracted from the model

for the snapshots of highest goodness for the diffuse gas. This corresponds to a peak of ram pressure occurred 140 Myr ago. Similarly to the deep Hα observations presented in Fossati et al. (2018), the model shows extra-planar linear filaments in the downwind region of the galactic disc, which correspond to the low-surface-brightness filaments located in the south-west tail and close to the downturn in the north-east (Vollmer et al. 2021). These filaments indicate the direction of the motion on the plane of the sky of the galaxy within the cluster.

The agreement between the gas distribution in the observations and in the simulations is overall very satisfactory. The brightest Hα knots detected in the FP observation (panel a) correspond to the brightest Hα regions in the simulation (panels b and c). The diffuse Hα emission in the model, given (in log scale) in panel b, is far too faint to be detected in the FP observations, but it matches fairly well the diffuse emission observed using the Hα narrow-band filter by Fossati et al. (2018). While the tuning is very good at the north-east edge of the disc, the simulated south-west tail has a larger curvature than that observed in the diffuse ionised gas detected by VESTIGE. This difference might be due to the fact that, given the orientation of NGC 4330 and its deduced orbit within the cluster, the north-east edge of the disc is the region of the galaxy that first suffered the stripping process.

As suggested by the simulations, all the diffuse gas component (mainly HI gas) has been already stripped, while that in the south-west direction, which was perturbed later, is still partly present, as suggested by the diffuse HI tail observed by Chung et al. (2007). This effect is probably combined with an asymmetric distribution of the star-forming regions over the disc of the galaxy, possibly formed after the external perturbation, with more compact HII regions along the south-west edge of the disc. Given their compactness and high density, these regions are less subject to the external perturbation than the diffuse gas. The difference between observations and simulations might thus result from a combined effect of sensitivity, gas density, and time elapsed since the beginning of the perturbation. Indeed, as shown in Fig. 19 of Abramson et al. (2011), the south-west curvature of the gas is more pronounced in the cold and diffuse atomic phase (the first one stripped) than in the compact Hα, more resistant to the external pressure.

The Hα LoS velocity fields are shown in panel a of Fig. 11. In order to compare the model to the data, a systemic velocity of 1551 km s^{-1} has been added to the model. The velocity amplitudes are the same for the three panels. Hα isocontours from Fossati et al. (2018), corresponding to a surface brightness of $\Sigma(\mathrm{H}\alpha) \sim 2 \times 10^{-18}$ erg s^{-1} cm^{-2} arcsec^{-2}, have been displayed in order to facilitate the comparison between the panels. We observe a very good agreement between the simulation and the observations. Where the simulations can be compared to the data, the amplitudes of the velocity fields are consistent. We note that if we include the low-surface-brightness tails, unfortunately not reached by the shallow FP observations, the velocity range in the simulations is even larger.

On the other hand, the HI velocity field (Fig. C.5, bottom panel) seems to show that the LoS velocities increase at the edge of the tail, although this rising is not very sharp, probably because of the lack of resolution in the HI data. The same excellent agreement is present also between the observed and simulated unfolded RCs shown in Fig. C.7 on which the simulated RC measured along the major axis of the galaxy has been compared to the GHASP observed and modelled RCs. The RC extracted from the simulations well predict the observed asymmetries between the receding (north-east) and approaching (south-west) sides of the disc up to ~70 arcsec (~5.6 kpc). Since the RC extracted from the simulations is taken on the major axis, we do not have any data outside this radius because the ionised gas emission is bent to the south-west.

The Hα LoS velocity dispersion fields are compared in the right panels of Fig. 11 using the same velocity range in the three panels. The mean velocity dispersion in the data is ~20.5 km s^{-1}, with a standard deviation of ~6.7 km s^{-1}, while in the model those quantities are respectively equal to ~10.6 and ~6.7 km s^{-1}. The smaller mean velocity dispersion in the model with respect to the observations (which have an instrumental limiting resolution of ~13 km s^{-1}), is due to the fact that the model estimate is strongly weighted by the diffuse gas component. This component is not reached by the observations. If we consider only the area of the model corresponding to the one detected in the data, the mean model velocity dispersion becomes ~17.5 km s^{-1}, with a standard deviation of ~6.4 km s^{-1}, and matches fairly well the observations. Striking is the similarity between models and observations around RA = $12^{\mathrm{h}}23^{\mathrm{m}}15.5^{\mathrm{s}}$, Dec = 11°21′42″, where the velocity dispersion increases by one sigma with respect to other regions along the galaxy disc up to 28–45 km s^{-1} in the data and 30–40 km s^{-1} in the model (in red in both cases).

8. Discussion and conclusion

Located in the nearby Virgo cluster, where 1 arcsec corresponds to ~80 pc, the edge-on late-type NGC 4330 is the perfect candidate for studying the effects of ram pressure stripping in the direction perpendicular to the disc plane of a perturbed system with an angular and spectral resolution unreachable elsewhere. The presence of extended tails in the atomic (Chung et al. 2007) and ionised (Fossati et al. 2018) gas and in the dust component (Longobardi et al. 2020) observed in this object testify to an ongoing stripping process that is able to remove the different phases of the ISM in the outer regions and produce a truncated disc.

Using two different and independent sets of FP observations with a spectral resolution of up to $R \sim 10\,000$, combined with our own tuned hydrodynamic simulations (Vollmer et al. 2021), we studied the kinematics of the ionised gas. Although the diffuse emission of the ionised gas in the stripped tails, which has a surface brightness of $\Sigma(\mathrm{H}\alpha) \simeq 3 \times 10^{-18}$ erg s^{-1} cm^{-2} arcsec^{-2}, has not been reached by the present observations, limited to $\Sigma(\mathrm{H}\alpha) \simeq 10^{-17}$ erg s^{-1} cm^{-2} arcsec^{-2}, our data allowed us to study the kinematics of the gas along the disc and in a few HII regions located outside the disc plane and probably formed within the stripped gas after the interaction.

The Fourier transform analysis of the deep NGVS i-band image reveals that the B_4 parameter is negative, indicating that the galaxy disc has a boxy shape outside a radius of ≃60 arcsec (≃4.8 kpc). This boxy structure is present mostly in the south-west direction, where the tail of stripped material is more pronounced. Simulations suggests that a thicker disc could result from the perturbation of the gravitational potential well due to the displacement of the gaseous component from the disc plane after a ram pressure stripping event (Farouki & Shapiro 1980; Clarke et al. 2017; Safarzadeh & Scannapieco 2017; Steyrleithner et al. 2020). The boxy shape would thus result from the induced perturbation on the stellar orbits. The datasets used in this work, which are sensitive only to the kinematics of the ionised gas, do not allow us to test this hypothesis. However, in the central regions, the kinematic major axis matches with the dust lane position angles, indicating that the perturbation

probably had only a moderate effect on the dynamics of the inner gas.

It is thus conceivable that the dynamics of the stars are also moderately perturbed. Indeed, within the inner stellar disc ($r \lesssim 2$ kpc), the velocity field of the galaxy dominated by the emission of HII regions is characterised by isovelocities parallel to the minor axis. The analysis of the RCs and of the PVDs consistently indicates a solid-body rotation. Outside this radius the isovelocities are bent, becoming parallel to the major axis, and show a low velocity gradient in the south-western edges of the disc, indicating non-circular motions.

The FP data allowed us to detect several ionised gas features formed after the dynamical interaction of the galaxy with the surrounding ICM (ram pressure) and located at the edges or outside the stellar disc. These are i) a hook-like structure at the north-east of the galaxy in the region that first came into contact with the ICM, and ii) several bright and extended regions formed along the downstream direction of the wind, principally located in the south-west of the galaxy, including a few HII regions well outside the disc and located along the filaments of stripped gas.

The analysis of the velocity field, of the velocity dispersion, of the RCs (derived using the ETM necessary to correct for beam smearing effects due to the velocity superposition along the LoS), and of the PVDs consistently indicates that these regions do not follow the solid-body rotation but have peculiar velocities indicative of streaming motions out of the plane of the galaxy. We also observe a small decrease in the rotation of the stripped gas with increasing distance from the galaxy disc.

This observational evidence can be explained considering that the stripping process is mainly perpendicular to the disc plane, as indeed suggested by our hydrodynamic simulations. Under this geometrical configuration, the gas is expected to keep its rotation with only a partial and gradual loss of angular momentum. Furthermore, the similarity of the Hα, CO, and HI velocity fields and RCs, particularly in the inner disc, indicates that here ram pressure stripping significantly affects the gas kinematics. Since in this scenario the acceleration caused by ram pressure is inversely proportional to the stripped gas surface density, the observed similarity in the kinematical perturbations of the different gas components (ionised, molecular, atomic) is expected given their comparable surface density.

Overall, the kinematical properties of the galaxy and of all these extraplanar features formed after the ram pressure stripping event are well reproduced by our simulations, at least up to the limited sensitivity of our FP observations. Nevertheless, it is hard to drive general conclusions regarding the effects of ram pressure stripping on the kinematical properties of galaxies and of the stripped material from the analysis of a single object.

The present results, however, combined with those obtained from the analysis of the kinematical properties of a few other well-resolved galaxies with available IFU data (e.g., Chemin et al. 2006; Merluzzi et al. 2013; Fumagalli et al. 2014; Consolandi et al. 2017; Boselli et al. 2022), consistently suggest that the gas removed during a ram pressure stripping event tends to keep its rotation, albeit with a possible loss of angular momentum. The perturbation can affect the kinematics of the gas even inside the disc of the perturbed system (Boselli et al. 2021). Although we still lack direct evidence, indirect observations and simulations consistently indicate that a ram pressure stripping event can also perturb, although to a lower extent, the kinematics of the stellar component. Deep IFU spectroscopic observations with a sufficient spectral resolution of perturbed systems will be required to probe this scenario.

Acknowledgements. Based on observations collected at the Observatorio Astronómico Nacional at San Pedro Mártir, Baja California, México (OAN - SPM). We thank the daytime and night support staff at the OAN-SPM for facilitating and helping obtain our observations. Also, based on observations taken with the GHASP and MISTRAL spectrographs at the Observatoire de Haute Provence (OHP, France), operated by the French CNRS. The authors warmly thank Olivier Boissin from LAM and the OHP team for its technical assistance before and during the observations, namely the night team: Jean Balcaen, Stéphane Favard, Jean-Pierre Troncin, Didier Gravallon and the day team led by François Moreau as well as Dr. Auguste Le Van Suu, the Head of Observatoire de Haute Provence-Institut Pythéas. We are grateful to the whole CFHT team who assisted us in the preparation and in the execution of the observations and in the calibration and data reduction: Todd Burdullis, Daniel Devost, Bill Mahoney, Nadine Manset, Andreea Petric, Simon Prunet, Kanoa Withington. We acknowledge financial support from "Programme National de Cosmologie and Galaxies" (PNCG) funded by CNRS/INSU-IN2P3-INP, CEA and CNES, France,and from "Projet International de Coopération Scientifique" (PICS) with Canada funded by the CNRS, France. This research has made use of the NASA/IPAC Extragalactic Database (NED), which is operated by the Jet Propulsion Laboratory, California Institute of Technology, under contract with the National Aeronautics and Space Administration and of the GOLDMine database (http://goldmine.mib.infn.it/) (Gavazzi et al. 2003). M. M. S. warmly thanks the Mexican National Council on Science and Technology (CONACyT) who found her through the program "Becas CONACyT al Extranjero 2017", CVU 666085, and to the Secretariat of Public Education (SEP) of the Mexican Government through the scholarship "Becas Complemento de Apoyo al Posgrado ciclo 2018-2019". M. R. thanks also the grants IN109919 of DGAPA-UNAM and CY-253085 and CF-86367 of CONACyT. M.B. acknowledges FONDECYT regular grant 1211000. A. L. is supported by Fondazione Cariplo, grant No. 2018-2329. M.F. acknowledges funding from the European Research Council (ERC) (grant agreement No. 757535).

References

Abramson, A., Kenney, J. D. P., Crowl, H. H., et al. 2011, AJ, 141, 164
Adami, C., Basa, S., Brunel, J. C., et al. 2018, in SF2A-2018: Proceedings of the Annual meeting of the French Society of Astronomy and Astrophysics, eds. P. Di Matteo, F. Billebaud, F. Herpin, et al., 357
Amram, P., Le Coarer, E., Marcelin, M., et al. 1992, A&AS, 94, 175
Barbosa, C. E., Mendes de Oliveira, C., Amram, P., et al. 2015, MNRAS, 453, 2965
Bellhouse, C., Jaffé, Y. L., Hau, G. K. T., et al. 2017, ApJ, 844, 49
Bellhouse, C., Jaffé, Y. L., McGee, S. L., et al. 2019, MNRAS, 485, 1157
Bizyaev, D., Walterbos, R. A. M., Yoachim, P., et al. 2017, ApJ, 839, 87
Boissier, S., Boselli, A., Duc, P. A., et al. 2012, A&A, 545, A142
Boselli, A., & Gavazzi, G. 2006, PASP, 118, 517
Boselli, A., & Gavazzi, G. 2014, A&ARv, 22, 74
Boselli, A., Boissier, S., Cortese, L., et al. 2006, ApJ, 651, 811
Boselli, A., Boissier, S., Cortese, L., & Gavazzi, G. 2008a, ApJ, 674, 742
Boselli, A., Boissier, S., Cortese, L., & Gavazzi, G. 2008b, A&A, 489, 1015
Boselli, A., Eales, S., Cortese, L., et al. 2010, PASP, 122, 261
Boselli, A., Cortese, L., & Boquien, M. 2014a, A&A, 564, A65
Boselli, A., Cortese, L., Boquien, M., et al. 2014b, A&A, 564, A66
Boselli, A., Fossati, M., Gavazzi, G., et al. 2015, A&A, 579, A102
Boselli, A., Cuillandre, J. C., Fossati, M., et al. 2016a, A&A, 587, A68
Boselli, A., Roehlly, Y., Fossati, M., et al. 2016b, A&A, 596, A11
Boselli, A., Fossati, M., Cuillandre, J. C., et al. 2018a, A&A, 615, A114
Boselli, A., Fossati, M., Ferrarese, L., & Boissier, S. 2018b, A&A, 614, A56
Boselli, A., Fossati, M., Consolandi, G., et al. 2018c, A&A, 620, A164
Boselli, A., Fossati, M., Longobardi, A., et al. 2019, A&A, 623, A52
Boselli, A., Lupi, A., Epinat, B., et al. 2021, A&A, 646, A139
Boselli, A., Fossati, M., Longobardi, A., et al. 2022, A&A, 659, A46
Byrd, G., & Valtonen, M. 1990, ApJ, 350, 89
Cappellari, M., & Copin, Y. 2003, MNRAS, 342, 345
Cárdenas-Martínez, N., & Fuentes-Carrera, I. 2018, ApJ, 868, 141
Carvalho, M. S., & Plana, H. 2018, MNRAS, 481, 122
Cayatte, V., van Gorkom, J. H., Balkowski, C., & Kotanyi, C. 1990, AJ, 100, 604
Chemin, L., Balkowski, C., Cayatte, V., et al. 2006, MNRAS, 366, 812
Chung, A., van Gorkom, J. H., Kenney, J. D. P., & Vollmer, B. 2007, ApJ, 659, L115
Chung, A., van Gorkom, J. H., Kenney, J. D. P., Crowl, H., & Vollmer, B. 2009, AJ, 138, 1741
Clarke, A. J., Debattista, V. P., Roškar, R., & Quinn, T. 2017, MNRAS, 465, L79
Consolandi, G., Gavazzi, G., Fossati, M., et al. 2017, A&A, 606, A83
Cortese, L., Davies, J. I., Pohlen, M., et al. 2010, A&A, 518, L49
Cortese, L., Ciesla, L., Boselli, A., et al. 2012a, A&A, 540, A52

Cortese, L., Boissier, S., Boselli, A., et al. 2012b, A&A, 544, A101
Cortese, L., Catinella, B., & Smith, R. 2021, PASA, 38
Courteau, S. 1997, AJ, 114, 2402
Cowie, L. L., & Songaila, A. 1977, Nature, 266, 501
Daigle, O., Carignan, C., Amram, P., et al. 2006a, MNRAS, 367, 469
Daigle, O., Carignan, C., Hernandez, O., Chemin, L., & Amram, P. 2006b, MNRAS, 368, 1016
Dressler, A. 1980, ApJ, 236, 351
Drew, P. M., Casey, C. M., Burnham, A. D., et al. 2018, ApJ, 869, 58
Epinat, B., Amram, P., & Marcelin, M. 2008a, MNRAS, 390, 466
Epinat, B., Amram, P., Marcelin, M., et al. 2008b, MNRAS, 388, 500
Erroz-Ferrer, S., Knapen, J. H., Font, J., et al. 2012, MNRAS, 427, 2938
Farouki, R., & Shapiro, S. L. 1980, ApJ, 241, 928
Ferrarese, L., Côté, P., Cuillandre, J.-C., et al. 2012, ApJS, 200, 4
Fossati, M., Fumagalli, M., Boselli, A., et al. 2016, MNRAS, 455, 2028
Fossati, M., Mendel, J. T., Boselli, A., et al. 2018, A&A, 614, A57
Fraternali, F., & Binney, J. J. 2006, MNRAS, 366, 449
Fuentes-Carrera, I., Rosado, M., Amram, P., et al. 2004, A&A, 415, 451
Fumagalli, M., Krumholz, M. R., Prochaska, J. X., Gavazzi, G., & Boselli, A. 2009, ApJ, 697, 1811
Fumagalli, M., Fossati, M., Hau, G. K. T., et al. 2014, MNRAS, 445, 4335
Gach, J.-L., Hernandez, O., Boulesteix, J., et al. 2002, PASP, 114, 1043
García-Ruiz, I., Sancisi, R., & Kuijken, K. 2002, A&A, 394, 769
Gavazzi, G., Catinella, B., Carrasco, L., Boselli, A., & Contursi, A. 1998, AJ, 115, 1745
Gavazzi, G., Boselli, A., Scodeggio, M., Pierini, D., & Belsole, E. 1999, MNRAS, 304, 595
Gavazzi, G., Boselli, A., Mayer, L., et al. 2001, ApJ, 563, L23
Gavazzi, G., Bonfanti, C., Sanvito, G., Boselli, A., & Scodeggio, M. 2002a, ApJ, 576, 135
Gavazzi, G., Boselli, A., Pedotti, P., Gallazzi, A., & Carrasco, L. 2002b, A&A, 396, 449
Gavazzi, G., Boselli, A., Donati, A., Franzetti, P., & Scodeggio, M. 2003, A&A, 400, 451
Gavazzi, G., Boselli, A., van Driel, W., & O'Neil, K. 2005, A&A, 429, 439
Gavazzi, G., Boselli, A., Cortese, L., et al. 2006, A&A, 446, 839
Gavazzi, G., Fumagalli, M., Cucciati, O., & Boselli, A. 2010, A&A, 517, A73
Gavazzi, G., Fumagalli, M., Fossati, M., et al. 2013, A&A, 553, A89
Gómez, P. L., Nichol, R. C., Miller, C. J., et al. 2003, ApJ, 584, 210
Gómez-López, J. A., Amram, P., Epinat, B., et al. 2019, A&A, 631, A71
Gooch, R. 1996, in Astronomical Data Analysis Software and Systems V, eds. G. H. Jacoby, & J. Barnes, ASP Conf. Ser., 101, 80
Gullieuszik, M., Poggianti, B. M., Moretti, A., et al. 2017, ApJ, 846, 27
Gunn, J. E., Gott, J., & Richard, I. 1972, ApJ, 176, 1
Gwyn, S. D. J. 2008, PASP, 120, 212
Haynes, M. P., & Giovanelli, R. 1984, AJ, 89, 758
Heald, G. H., Rand, R. J., Benjamin, R. A., Collins, J. A., & Bland-Hawthorn, J. 2006, ApJ, 636, 181
Heald, G. H., Rand, R. J., Benjamin, R. A., & Bershady, M. A. 2007, ApJ, 663, 933
Jáchym, P., Combes, F., Cortese, L., Sun, M., & Kenney, J. D. P. 2014, ApJ, 792, 11
Jáchym, P., Sun, M., Kenney, J. D. P., et al. 2017, ApJ, 839, 114
Jáchym, P., Kenney, J. D. P., Sun, M., et al. 2019, ApJ, 883, 145
Jedrzejewski, R. I. 1987, MNRAS, 226, 747
Junais, S., Boissier, A., Boselli, M., et al. 2021, A&A, 650, A99
Kalberla, P. M. W., Kerp, J., Dedes, L., & Haud, U. 2014, ApJ, 794, 90
Korsaga, M., Epinat, B., Amram, P., et al. 2019, MNRAS, 490, 2977
Kronberger, T., Kapferer, W., Ferrari, C., Unterguggenberger, S., & Schindler, S. 2008, A&A, 481, 337
Larson, R. B., Tinsley, B. M., & Caldwell, C. N. 1980, ApJ, 237, 692
Lee, B., Chung, A., Tonnesen, S., et al. 2017, MNRAS, 466, 1382
Lequeux, J. 1983, A&A, 125, 394
Levy, R. C., Bolatto, A. D., Sánchez, S. F., et al. 2019, ApJ, 882, 84
Lewis, I., Balogh, M., De Propris, R., et al. 2002, MNRAS, 334, 673
Longobardi, A., Boselli, A., Fossati, M., et al. 2020, A&A, 644, A161
Mei, S., Blakeslee, J. P., Côté, P., et al. 2007, ApJ, 655, 144
Merluzzi, P., Busarello, G., Dopita, M. A., et al. 2013, MNRAS, 429, 1747
Merritt, D. 1983, ApJ, 264, 24
Mihalas, D., & Binney, J. 1981, Galactic astronomy: Structure and Kinematics, 2nd edn. (W H Freeman & Co.)
Miller, S. T., & Veilleux, S. 2003, ApJ, 592, 79
Mo, H., van den Bosch, F. C., & White, S. 2010, Galaxy Formation and Evolution (Cambridge University Press)
Moiseev, A. V. 2014, Astrophys. Bull., 69, 1
Moiseev, A. V., & Lozinskaya, T. A. 2012, MNRAS, 423, 1831
Moore, B., Lake, G., & Katz, N. 1998, ApJ, 495, 139
Moretti, A., Paladino, R., Poggianti, B. M., et al. 2020, ApJ, 897, L30
Munoz-Tunon, C., Tenorio-Tagle, G., Castaneda, H. O., & Terlevich, R. 1996, AJ, 112, 1636
Osterbrock, D. E., Fulbright, J. P., Martel, A. R., et al. 1996, PASP, 108, 277
Osterbrock, D. E., & Ferland, G. J. 2006, Astrophysics of Gaseous Nebulae and Active Galactic Nuclei (University Science Books)
Peng, Y.-J., Lilly, S. J., Kovač, K., et al. 2010, ApJ, 721, 193
Poggianti, B. M., Gullieuszik, M., Tonnesen, S., et al. 2019, MNRAS, 482, 4466
Quilis, V., Moore, B., & Bower, R. 2000, Science, 288, 1617
Roediger, E., & Hensler, G. 2005, A&A, 433, 875
Rosado, M., Langarica, R., Bernal, A., et al. 1995, Rev. Mex. Astron. Astrofis. Conf. Ser., 3, 263
Rosado, M., Gabbasov, R. F., Repetto, P., et al. 2013, AJ, 145, 135
Safarzadeh, M., & Scannapieco, E. 2017, ApJ, 850, 99
Sancisi, R., & Allen, R. J. 1979, A&A, 74, 73
Sardaneta, M. M., Rosado, M., & Sánchez-Cruces, M. 2020, Rev. Mex. Astron. Astrofis., 56, 71
Sheen, Y.-K., Smith, R., Jaffé, Y., et al. 2017, ApJ, 840, L7
Sofue, Y., & Rubin, V. 2001, ARA&A, 39, 137
Sofue, Y., Tutui, Y., Honma, M., & Tomita, A. 1997, AJ, 114, 2428
Sofue, Y., Tomita, A., Honma, M., & Tutui, Y. 1999a, PASJ, 51, 737
Sofue, Y., Tutui, Y., Honma, M., et al. 1999b, ApJ, 523, 136
Solanes, J. M., Manrique, A., García-Gómez, C., et al. 2001, ApJ, 548, 97
Spector, O., Finkelman, I., & Brosch, N. 2012, MNRAS, 419, 2156
Steyrleithner, P., Hensler, G., & Boselli, A. 2020, MNRAS, 494, 1114
Sun, M., Donahue, M., & Voit, G. M. 2007, ApJ, 671, 190
Swaters, R. A., Sancisi, R., & van der Hulst, J. M. 1997, ApJ, 491, 140
Takamiya, T., & Sofue, Y. 2000, ApJ, 534, 670
Takamiya, T., & Sofue, Y. 2002, ApJ, 576, L15
Tonnesen, S., & Bryan, G. L. 2009, ApJ, 694, 789
Valdez-Gutiérrez, M., Rosado, M., Georgiev, L., Borissova, J., & Kurtev, R. 2001, A&A, 366, 35
Vollmer, B., Cayatte, V., Balkowski, C., & Duschl, W. J. 2001, ApJ, 561, 708
Vollmer, B., Beck, R., Kenney, J. D. P., & van Gorkom, J. H. 2004, AJ, 127, 3375
Vollmer, B., Soida, M., Otmianowska-Mazur, K., et al. 2006, A&A, 453, 883
Vollmer, B., Braine, J., Pappalardo, C., & Hily-Blant, P. 2008, A&A, 491, 455
Vollmer, B., Soida, M., Braine, J., et al. 2012, A&A, 537, A143
Vollmer, B., Fossati, M., Boselli, A., et al. 2021, A&A, 645, A121
Wakker, B. P., & van Woerden, H. 1997, ARA&A, 35, 217
Warner, P. J., Wright, M. C. H., & Baldwin, J. E. 1973, MNRAS, 163, 163
Weiner, B. J., Willmer, C. N. A., Faber, S. M., et al. 2006, ApJ, 653, 1027
Yagi, M., Yoshida, M., Komiyama, Y., et al. 2010, AJ, 140, 1814
Zhao, Q., Sun, L., Shen, L., et al. 2021, ApJ, 913, 111
Zschaechner, L. K., & Rand, R. J. 2015, ApJ, 808, 153
Zschaechner, L. K., Rand, R. J., & Walterbos, R. 2015, ApJ, 799, 61

Appendix A: Fabry-Perot observations

A.1. PUMA observations

Three-dimensional FP spectroscopic observations of NGC 4330 were gathered using PUMA at the 2.1 m telescope at the Observatorio Astronómico Nacional in San Pedro Mártir, Baja California, Mexico (OAN-SPM; Rosado et al. 1995). The PUMA focal reducer hosts an FP interferometer with a field of view of $\sim 10 \times 10$ arcmin^2. The camera is a 512×512 CCD detector[3] with a pixel scale of $\sim 1.27 \times 1.27$ arcsec^2.

NGC 4330 was observed during dark time, in February 2017[4] (see Table 1), as part of the FP survey of the *Herschel* Reference Survey (Boselli et al. 2010; Gómez-López et al. 2019). To increase the S/N, the pixels have been electronically rebinned by 4×4, leading to a final spatial sampling of ~ 1.3 arcsec. The galaxy was observed during poor seeing conditions ($FWHM \sim$ 2.9±0.3 arcsec) but excellent transparency with a total exposure time of 96 min, with 120 seconds per channel. The spectral domain has been selected using a $FWHM = 90$ Å wide filter centred at 6607 Å. The spectroscopic calibration of the data was made using the narrow Ne line at 6598.95 Å in the same interference filter. The choice of this line is optimal to minimise the phase shift effects due to the coating of the interferometer since it is very close to the redshifted Hα emission line of the galaxy (~6597 Å). The theoretical PUMA effective finesse is $F \sim 24$ but the one measured using the narrow Ne spectral line was $F_e \sim 19.9$. The FP interference order at the mean wavelength of the observation is $p \sim 328$, which gives a resolution $R = p\,F_e \sim 6533$. The free spectral range (FSR) of the instrument at the redshifted wavelength of the galaxy, ~20.04 Å (911 km s^{-1}), was scanned through 48 channels, corresponding to a spectral sampling of ~ 0.42 Å (19 km s^{-1}). The instrumental and observational parameters are listed in Table A.1.

Standard corrections were applied to the CCD images. The astrometric calibration of the data has been done using the KOORDS task of the KARMA[5] package (Gooch 1996) and WCS (Word Coordinate System) textscIRAF[6] task. The FP data were reduced and analysed using the ADOCHw [7] software, the IDL-based COMPUTEEVERYTHING [8], REDUCWIZARD interface [9], and our own PYTHON scripts.

The filter includes the Hα line and the [NII] lines at 6548.03 and 6583.48 Å (see Fig. C.1). Since the FSR of the interferometer is ~ 4.5 times smaller than the filter width, the [NII] lines are present in the data cube but are respectively observed at the interference order $p + 1$ and $p - 1$ with respect to Hα, which is observed at order p. Furthermore, the apparent separation between Hα and [NII]6548 lines is ~+5.0 Å and the one with the [NII]6583 is ~+0.9 Å , as illustrated in the bottom panel of Fig. C.1.

Since the spectral resolution at Hα redshifted is ~1.01 Å, the [NII]6548 line is resolved from the Hα line while the [NII]6583 line partially overlaps with Hα, affecting the barycentre position and the line width measurements of the Hα line. In order to correct for this effect, we make a model that takes into account (i) a constant line ratio of [NII]6583/Hα = 0.35, as measured using the VLT/FORS long slit spectrum published in Fossati et al. (2018), (ii) the known wavelength separation of ~20.73 Å (~ 942 km s^{-1}) between the redshifted Hα and [NII]6583 lines, and (iii) the Hα_0 FSR at rest ~19.8Å (~ 905 km s^{-1}). Considering that the dispersion of the instrumental line spread function (LSF) is $\sigma_{\rm LSF}$ ~ 0.43 Å (~ 19.5 km s^{-1}), the thermal broadening $\sigma_{\rm T}$ ~ 0.18 Å (~9.1 km s^{-1}), and the intrinsic mean velocity dispersion σ ~ 0.44 Å (~ 20.0 km s^{-1}), the model indicates that the observed Hα barycentre and the velocity dispersion should be corrected by -0.20 Å (-8.9 km s^{-1}) and -0.12 Å (-5.3 km s^{-1}), respectively.

We computed a parabolic phase map from the calibration cube in order to obtain the reference wavelength for the line profile observed inside each pixel. This phase map provides the shift that has to be applied in the spectral dimension to every pixel of the interferogram cube to bring all channels to the same wavelength. The wavelength-sorted data cube is then created by applying the phase map correction to the interferogram data cube. A detailed explanation about the data reduction process for data obtained at OAN-SPM with PUMA can be found in Fuentes-Carrera et al. (2004).

In order to work with profiles and maps with a similar S/N and at the same time optimise the angular resolution, we applied a Voronoi tessellation with a constant S/N = 9 to the data cube Cappellari & Copin (2003), Daigle et al. (2006a,b). The brightest HII regions are not affected by this smoothing procedure because their S/N per pixel is larger than 9 and are thus displayed at full resolution.

The resulting data cubes are used to extract the monochromatic, continuum, LoS radial velocity and velocity dispersion maps of the galaxy. The continuum map is computed considering the average of the 3 lowest intensities of the 48 channels of the cube. For the monochromatic image, the intensity of the Hα line is obtained by integrating the flux of the line profile for each pixel. Following Daigle et al. (2006a), we calculate the radial velocity in each pixel by measuring the barycentre of the profile of the Hα line. This barycentre is computed as the intensity weighted centroid of the spectral bins falling into the emission line boundaries, with the continuum subtracted. Radial velocities and velocity dispersions are extracted using a single emission-line detection algorithm. In the case where more than one velocity component is present in the spectrum, only the strongest emission line is taken into account. When two emission lines are spectrally close and have comparable amplitudes, they might be taken as a single one with a larger velocity dispersion.

Assuming that all the Hα emission-profiles are described by Gaussian functions, from the emission profiles width map the velocity dispersion σ was estimated as

$$\sigma = (\sigma^2_{\rm LoS} - \sigma^2_{\rm LSF} - \sigma^2_{\rm T})^{1/2}, \quad \text{(A.1)}$$

where $\sigma_{\rm LoS}$ is the observed LoS velocity dispersion directly measured from the data cube corrected (i) from the instrumental LSF (e.g. Valdez-Gutiérrez et al. 2001; Rosado et al. 2013; Cárdenas-Martínez & Fuentes-Carrera 2018), which is modelled using the instrumental finesse F and the FSR by $\sigma_{\rm LSF}$ = FSR/

[3] The PUMA CCD has in fact 2048×2048 px^2, which are electronically binned 4×4 to increase the S/N per pixel by a factor of 16 and to take into account the mean seeing of the site.
[4] Additional deeper PUMA observations of NGC 4330 could not be made due to the lockdown in spring 2020 (northern emisphere).
[5] https:www.atnf.csiro.au/computing/software/karma/
[6] 'Image Reduction and Analysis Facility', http://iraf.noao.edu/; IRAF is distributed by the National Optical Astronomy Observatories, which are operated by the Association of Universities for Research in Astronomy, Inc., under cooperative agreement with the National Science Foundation.
[7] ADHOCw, http://cesam.lam.fr/fabryperot/index/softwares, developed by J. Boulesteix.
[8] https://projets.lam.fr/projects/computeeverything
[9] https://projets.lam.fr/projects/fpreducwizard

Table A.1. Set-up of the FP observations.

Parameter	OAN-SPM	OHP	
Telescope	2.1 m	1.93 m	
Instrument	PUMA[(1)]	GHASP	
Seeing	2.9 arcsec	2.5 - 4.5 arcsec	
Galaxy Hα wavelength range	6593 - 6600 Å		
velocity range	1380 - 1672 km s^{-1}		
Observation date	2017-02-23	2021-01-14 to 18 2021-02-11	2021-01-16 to 18
Number of cycles	1	80	37
Total exposure time	96 min	427 min	200 min
Scanning FP interferometer	ICOS - ET-50[(2)]		
Calibration (Neon line)	6598.95 Å		
Finesse (F)	19.9	12.3±0.3[(3)]	
p[(4)] at H$\alpha_0^{(5)}$=6562.8 (H$\alpha^{(5)}$= 6596.8Å)	330 (328)	793 (789)	
Resolution power (pF) at H$\alpha^{(5)}$	6533	9704±25	
Free spectral range at H$\alpha^{(5)}$	20.05 Å / 911 km s^{-1}	8.35 Å / 379 km s^{-1}	
Spectral resolution at H$\alpha^{(5)}$	1.01 Å / 45.8 km s^{-1}	0.68 Å / 30.9 km s^{-1}	
Spectral sampling at H$\alpha^{(5)}$	0.42 Å / 19.0 km s^{-1}	0.26 Å / 11.9 km s^{-1}	
Line spread function ($\sigma_{\rm LSF}$)	0.43 Å / 19.5 km s^{-1}	0.29 Å / 13.1 km s^{-1}	
Scanning steps	48	32	
Exposure time per channel	120 s	10 s	
Detector Name	Spectral 2 [(6)]	IPCS (GaAs)	
Detector size	512 × 512 pixels^2	512 × 512 pixels^2	
Field-of-view	10 × 10 arcmin^2	5.8 × 5.8 arcmin^2	
Image scale	1.27[(7)] arcsec pix^{-1}	0.68[(8)] arcsec pix^{-1}	

Notes. [(1)] https://www.astrossp.unam.mx/instrumentos/interferometria/puma/docs/manualespuma/puma.html. [(2)] *Queensgate Instruments*, which is now called *IC Optical Systems*. [(3)] Mean and standard deviation of the finesse (F) measured from eight different calibration cubes. [(4)] p is the interference order. [(5)] Hα_0 is the wavelength of the Hα-line at rest, and Hα the wavelength at the galaxy heliocentric LoS velocity (see Table 1). [(6)] https://www.astrossp.unam.mx/en/users/ccd-s. [(7)] After 4 ×4 electronic binning on the CCD. [(8)] After 2 ×2 electronic binning on the IPCS.

(F × 2$\sqrt{2\ln 2}$) ~19.5 km s^{-1} (see Table A.1) and (ii) from the thermal broadening $\sigma_{\rm T} = (kT_e/m_{\rm H})^{1/2} = 9.1$ km s^{-1}, assuming an electronic temperature of HII regions of $T_{\rm e} = 10^4$ K (Osterbrock & Ferland 2006).

A.2. GHASP observations

An independent set of FP spectroscopic observations was taken using the GHASP instrument on the 1.93 m telescope at the OHP in spring 2021 (northern emisphere). These observations were gathered using the same configuration extensively described in Gómez-López et al. (2019). The GHASP focal reducer is equipped with an FP with a field of view of 5.8 × 5.8 arcmin^2 and a 512 × 512 Imaging Photon Counting System[10] with a pixel scale of 0.68 × 0.68 arcsec^2 (Gach et al. 2002). The observations were taken during poor seeing conditions (2.5 < $FWHM$ < 4.0 arcsec), with medium transparent sky, and with a total integration time of 645 minutes. The FSR of the FP at the redshifted wavelength of the galaxy (379 km s^{-1}) was scanned through 32 channels, with a typical spectral resolution of R ~9704 at Hα redshifted. NGC 4330 was observed using two different narrow-band interference filters. Indeed, the mean redshifted Hα wavelength of the galaxy is ~ 6597 Å, which unfortunately falls just in the middle of two available interference filters centred on 6591 Å and 6601 Å. Both filters have the same $FWHM$ ~15 Å useful to overcome [NII] line contamination. To cover the whole velocity field of the galaxy, the first filter was used for the blueshifted part of the galaxy, the second one for the redshifted side. This does not exactly double the observing time because approximatively two-thirds of the velocity amplitude was covered by the two filters that overlap by ~5 Å. Similarly to the PUMA observation, the wavelength calibrations were done using the NeI emission line at λ = 6598.95 Å. The data reduction procedure adopted to reduce the GHASP data have been extensively described in Epinat et al. (2008b) and Gómez-López et al. (2019). The LoS velocity dispersion has been corrected from the LSF and thermal broadening using the method and the relations described in the previous section (Sect. A.1). The main observational parameters of the FP observations are summarised in Table A.1.

We decided not to combine the FP observations obtained with GHASP and PUMA because of their different spatial and spectral resolutions. On the contrary, we decided to keep them separated to i) check the consistency of the results in particular in the low-surface-brightness regions where the signal-to-noise is limited, ii) take benefit of the slightly better angular resolution of the PUMA data for the study of the extraplanar gas, and iii) of the higher spectral resolution of the GHASP data for the study of the velocity dispersion of the gas, and finally iv) use the deeper GHASP data for the comparison with the output of the simulations. We notice that for these purposes the observations were analysed differently: using a Voronoi adaptive spatial

[10] The GHASP image photon counting system (IPCS) has in fact 1024 × 1024 px^2, which are electronically binned 2×2 to increase by a factor of four the frame readout frequency and to take into account the mean seeing of the site. We remember that for an IPCS the S/N does not increase with the pixel binning.

smoothing for the PUMA data in order not to thicken the almost edge-on disc of the galaxy, while using a Gaussian smoothing for the GHASP observations to detect the weakest structures.

The different data cubes and maps presented in the next sections were thresholded using the VESTIGE image; all pixels below a surface brightness limit of 1 and 3.5×10^{-17} erg s^{-1} cm^{-2} arcsec^{-2}, for GHASP and PUMA, respectively, have been masked. Nevertheless, because of the night sky lines contamination, for the GHASP data, even above this threshold limit, it was not possible to calculate a consistent line flux nor velocity, and velocity dispersion for each pixel in the regions labelled B, C, D, H, J (western tail only) and M. For each region, the profiles were summed to give average values, which in turn lead to average flux, LoS, and velocity dispersions.

Appendix B: Derivation of the rotation curve

B.1. Position velocity diagrams

In order to study the velocity distribution as a function of the Hα surface brightness, we built PVDs from the FP data cube after having subtracted the stellar continuum (e.g. Epinat et al. 2008b; Rosado et al. 2013). Using a pseudo-slit of 2 pixels in width (i.e. ~2.6/1.4 arcsec for PUMA/GHASP, close to or below the seeing) centred at the photometric centre and aligned to the major axis defined in Sect. 3, we extracted the emission intensity projected along the major axis of the galaxy after rotating the data cube in order to align the position angle of the galaxy with the north-south direction (see Figure 8). We modified the *PA* and the centre of the pseudo-slit in order to obtain the most symmetric PVD in intensity, the final values correspond to the kinematic major axis (PA_{kin}) and kinematic centre (see Table B.1).

B.2. The intensity-peak method

The IPM is based either on a barycentric measurement of the line profiles for each pixel or by fitting it with a theoretical function such as a Gaussian (e.g. Sofue & Rubin 2001; Rosado et al. 2013). With this method, the tangential velocity in the galactic plane, V_{rot}, is computed under the assumption that the galaxy has an infinitesimally flat disc, inclined by an angle i with respect to the sky plane and dominated by rotational motions around an axis perpendicular to the galactic plane. Assuming an axial symmetry about the galactic centre and considering that the velocity field is dominated by circular motions, we can measure the velocity of the pixels that are at the same distance from the kinematic centre along the major axis by dividing the galaxy on the sky-plane into rings. The rotation velocity $V_{rot}(r)$ for a ring of radius r is given as the azimuthal average over the ring of the deprojected velocities:

$$V_{rot}(r, \theta) = \frac{V_{\rm LoS}(r, \theta) - V_{sys}}{\cos\theta \sin i}, \tag{B.1}$$

where r and θ are the radial and angular coordinates in the plane of the galaxy (Mihalas & Binney 1981) and $V_{\rm LoS}(r, \theta)$ is the LoS velocity extracted from each pixel of the FP velocity field (e.g. Fuentes-Carrera et al. 2004; Epinat et al. 2008a; Cárdenas-Martínez & Fuentes-Carrera 2018; Sardaneta et al. 2020).

This method has been used for the PUMA and GHASP datasets; the results are shown by the black filled and open squares in Fig. 3. In both cases, the RCs were computed considering all the pixels located within an angular sector of ±5° from the kinematic major axis, V_{rot} have been computed within circular rings of 6.5 arcsecond a galaxy kinematical inclination $i = 88°$. Both sides of each RC show a slowly rising solid-body shape despite the fact that both sides do not match outside the inner radius r_0 ~30 arcsec (~2.4 kpc), but the increasing trend of the curve continue up to ~95 arcsec (~8 kpc). We have indicated r_0 by dashed lines in all the maps and PVDs all over the paper. Beyond this radius, differences are observed between the receding and approaching sides. Discrepant points are associated with several regions previously identified in Fig. 2: region A on the hook-like structure and region J located at about the same galactocentric distance show a velocity discrepancy of ~110 km s^{-1} in the GHASP RC and ~50 km s^{-1} in the PUMA RC; regions K and L in the south-west tail do not have a counterpart on the other side of the galaxy. The deepest GHASP data show velocities fairly constant ($V_{rot} \sim 122 \pm 10$ km s^{-1}) in the south-west tail, consistent with a streaming motion.

B.3. The envelope-tracing method

The ETM uses the PVD traced along the major axis of the galaxy to simulate a pseudo-slit that has a width equal to two pixels (see Sect. B.1) and adopts all the kinematic parameters (centre, position angle, and systemic velocity; see Table B.1) derived from it, with the exception of the inclination, which cannot be determined using this method. Following Sofue et al. (1997, 1999a), García-Ruiz et al. (2002), the rotation velocity is defined as

$$V_{\rm rot} \sin i = (V_{\rm env} - V_{\rm sys}) - (\sigma_{\rm T}^2 + \sigma_{\rm LSF}^2)^{1/2}, \tag{B.2}$$

where $V_{\rm sys}$ is the systemic velocity, i is the galaxy inclination with respect to the sky plane, $\sigma_{\rm LSF}$ is the instrumental velocity dispersion, $\sigma_{\rm T}$ is the thermal broadening of the gas, and $V_{\rm env}$ is the terminal velocity characterised by the intensity of the envelope of an observed PVD along the line profile[11]. The intensity of the envelope is defined as

$$I_{\rm env} = [(\eta I_{\rm max})^2 + (I_{\rm min})^2]^{1/2}, \tag{B.3}$$

where $I_{\rm max}$ is the maximum intensity in the line profile, $I_{\rm min}$ is a minimum value of the contour, typically taken to be $3 \times rms$ noise in the PVD, and η is a constant that determines the fraction of maximum intensity to set the envelope intensity, which is usually taken in the range 0.2 − 0.5 (see references above). An arc-tangent model reproduces fairly well the shape of the envelope of the PVD with the smallest number of arguments and provides an adequate match to most RCs (Courteau 1997). This function is given by

$$V_{\rm env}(r) = V_{\rm sys} + V_0 \tan^{-1}\left(\frac{r - r_0}{r_t}\right) + C, \tag{B.4}$$

where $V_{\rm sys}$, V_0, r_0, r_t and C are five free parameters: V_{sys} is the systemic velocity, V_0 is the velocity amplitude with respect to the velocity C at $r = r_0$, r_0 and r_t are two characteristic radii that shape the curve marking the radius between the rising and flat part of the RC and the sharpness of this transition, respectively. r_0 is indeed the inflection point of the function visible on the purple curve on Fig. 3, and represented by two dashed lines on the Hα velocity fields (Fig. 5). This arc-tangent model has also been used by other authors Weiner et al. (2006), Drew et al. (2018),

[11] Sofue & Rubin (2001) provide a slightly different expression that corrects for instrumental and thermal broadening after deprojecting from inclination. Despite their work often being cited as reference since then, we believe this was a typo since the term that needs to be corrected for broadening is the observable, $V_{\rm env} - V_{\rm sys}$, as done in the previous work of Sofue et al. (1997).

Table B.1. Photometric and kinematic parameters.

Parameter	Photometric	Kinematic	
		PUMA	GHASP
C_α (J2000)[1]	$12^h23^m17.1^s$	$12^h23^m17.0^s$	$12^h23^m17.0^s$
C_δ (J2000)[1]	$+11°\ 22'\ 5.7''$	$+11°22'06.7''$	$+11°22'06.7''$
PA (deg)[2]	59.0 ± 0.1	56 ± 1	59 ± 1
i (deg)[3]	89.5 ± 0.1	88 ± 2	88 ± 2
V_{sys} (km s^{-1})[4]	...	1569 ± 2	1563 ± 2
V_{rot}^{ETM} (km s^{-1})[5]	...	164 ± 11	158 ± 8
V_{rot}^{ITM} (km s^{-1})[6]	...	162 ± 8	150 ± 21
$\langle\sigma_{obs}\rangle$ (km s^{-1})[7]	...	35 ± 10	21 ± 7
σ_{LSF} (km s^{-1})[8]	...	19.5	13.1
V_0^{ETM} (km s^{-1})[9]	...	46 ± 8	34 ± 5
r_0^{ETM} (arcsec)[10]	...	27 ± 2	28 ± 2
r_t^{ETM} (arcsec)[11]	...	17 ± 4	15 ± 4
C^{ETM} (km s^{-1})[12]	...	98 ± 3	100 ± 2
V_0^{ITM} (km s^{-1})[13]	...	107 ± 5	110 ± 15
r_t^{ITM} (arcsec)[14]	...	8 ± 3	20 ± 1

Notes. (1): Right ascension and declination of the galaxy centre. The photometric and the kinematic centre differ by less than half the seeing disc. (2): Position angle of the major axis. (3): Column 2: photometric inclination computed with the ELLIPSE task from IRAF. Columns 3 and 4: kinematic inclination computed with the ITM. (4): Systemic velocity. (5): Rotation velocity measured with the RC computed with the ETM at $R_{23.5}$. (6): Rotation velocity measured with the RC computed with the ITM at $R_{23.5}$. (7): Mean velocity dispersion. (8): Instrumental velocity dispersion (also called the LSF). (9) to (14): Best fit parameters of equation B.4 to compute the RC with the ETM (see text).

Zhao et al. (2021). Because the PVD is traced along the major axis, relation (B.4) can be transformed into a RC using relation (B.2). Therefore, to apply the ETM, we determined the terminal velocity $V_{\rm env}$ by fitting the arc-tangent model to both the maximum I_{max} and minimum I_{min} intensity line profiles. We corrected the velocities for $\sigma_{\rm LSF}$ for both instruments (see Table B.1) and for $\sigma_{\rm T} = 9.1\,{\rm km\,s^{-1}}$ to account for the dispersion due to the gas temperature along the LoS (see Sect. 2). The results of the ETM are shown in Fig. 3. The rotation velocities and its best fit are given on the upper panels a and c while the PVDs from which the rotation velocities have been computed are shown on the lowest panel b and d. Using Eq. (B.3), we computed the intensity of the envelope ($I_{\rm env}$) for η=[0.2-0.5] and then we applied relation (B.2). The shaded area corresponds to η=[0.2-0.5] and the purple curve to η=0.3. For η=0.3, the maximum coefficient of determination is $R^2 = 0.8$ and was obtained with the parameters given in Table B.1.

B.4. The iteration method

The IPM and the ETM are limited by the observational parameters such as the seeing, the spectral resolution, the slit width (or pseudo-slit width in case of two-dimensional velocity fields). They also depend on the physical properties of the galaxy such as its inclination, the velocity dispersion of the gas and its distribution within the disc. To overcome these sources of uncertainties, Takamiya & Sofue (2000) proposed a different model, the ITM, to generate a model data cube using specific radial and vertical density profiles of the ionised gas (e.g. exponentially declining), RCs, velocity dispersions, and viewing angles. First, to provide the initial conditions from which a first model data cube is computed, we used a RC derived from a PVD. Second, the ETM is used to derive a new RC from the first model data cube, which is compared to the data. Third, the differences between these two RCs are added to the input RC to generate a new model. This procedure is repeated until the difference between the RCs derived from the data and the final model satisfies a convergence criterion or until a maximum number of iterations has been performed (e.g. Takamiya & Sofue 2000; Sofue & Rubin 2001; Heald et al. 2006, 2007). As suggested by the intensity-weighted and the envelope-tracing RCs of NGC 4330, the inner regions of the disc within R_{23} show a solid-body shape (see Fig. 3 and 5).

Therefore, following Swaters et al. (1997), Heald et al. (2006), Rosado et al. (2013) and Moiseev (2014), we applied to NGC 4330 the classically called cylindrical model. This model assumes, as a first grade approximation, that the galaxy has the shape of a cylinder that rotates as a rigid body around the z axis perpendicular to the x, y plane, which defines the disc. In order to compute the model data cube, we proposed an initial RC that describes the rotation of the cylindrical shaped rigid body based on the arc-tangent model of a RC (Eq. B.4). Using the non-linear least-squares minimisation of the library LMFIT from PYTHON, we computed a model data cube for each FP dataset whose emission profiles were represented by Gaussian functions. The velocity dispersion of the emission peaks was fixed for all profiles to the medium value of the velocity dispersion of the galaxy $\langle\sigma_{\rm LoS}\rangle$. For the amplitude of the Gaussian functions, we assumed that the gas has an exponentially declining distribution (Mo et al. 2010; Takamiya & Sofue 2002) within the disc of the galaxy along the z direction, $B(z) = B_0 \exp(-|z|/z_d)$, and we measured the vertical disc length $z_d = 6$ arcsec using the Hα surface brightness distribution. We used the value of the kinematic centre of each dataset as the systemic velocity of the galaxy (V_{sys}) and the kinematic PA obtained from the PVDs. This implies that the free parameters of the model are: the transition radius between the rising and flat part of the RC (r_t), the asymptotic velocity (V_0), and the inclination (i) of the galaxy.

Appendix C: Additional figures

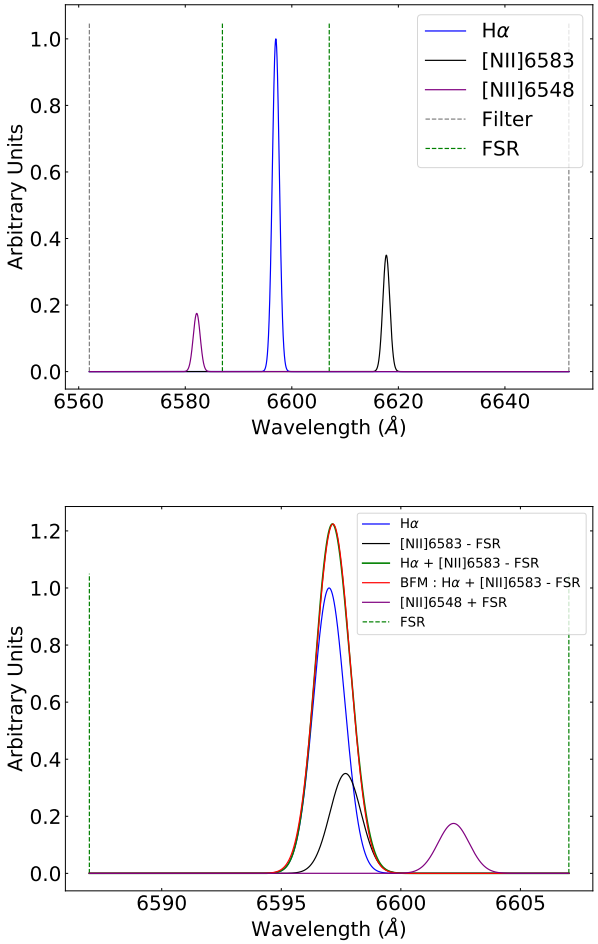

Fig. C.1. Model of the PUMA spectrum. The Hα plus the two [NII]6548, 6583 lines, transmitted by the filter, are represented by Gaussian functions of width $\sigma_{\rm LSF}$ (see Table 1). Normalised units to the Hα line are used for the y axis. The relative intensity between the Hα and the [NII] lines are given in Sect. A.1. The distance between the two green dashed vertical lines represents the FSR (~ 20 Å). Top panel: Redshifted Hα and [NII]6548, 6583 lines are located at their right position. The distance between the two grey dashed vertical lines represents the filter width ($FWHM \sim 90$ Å). Bottom panel: Redshifted lines located at their apparent position due to the FSR recovering. The [NII]6548 line is shifted by plus one FSR, and the [NII]6583 is shifted by minus one FSR. The green curve represents the sum of the Hα plus [NII]6583 lines, whereas the red one represents the Gaussian that best fits the sum of the two lines (best fit method).

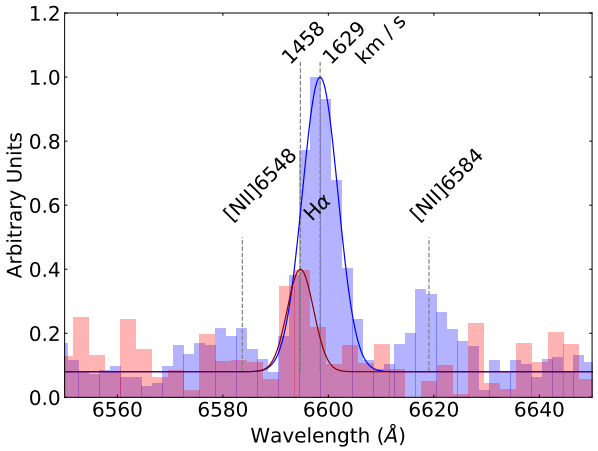

Fig. C.2. Long-slit spectra obtained with MISTRAL at the 1.93 m OHP telescope. The Hα lines of region D (red spectrum) and the position of the orthogonal projection of region D on the major axis of the galaxy (blue spectrum) are fitted by Gaussian functions, with intensities in normalised units. The two vertical dashed lines on Hα indicate the measured velocity of region D (1458±46 km s^{-1}) and on the disc (1629±46 km s^{-1}).

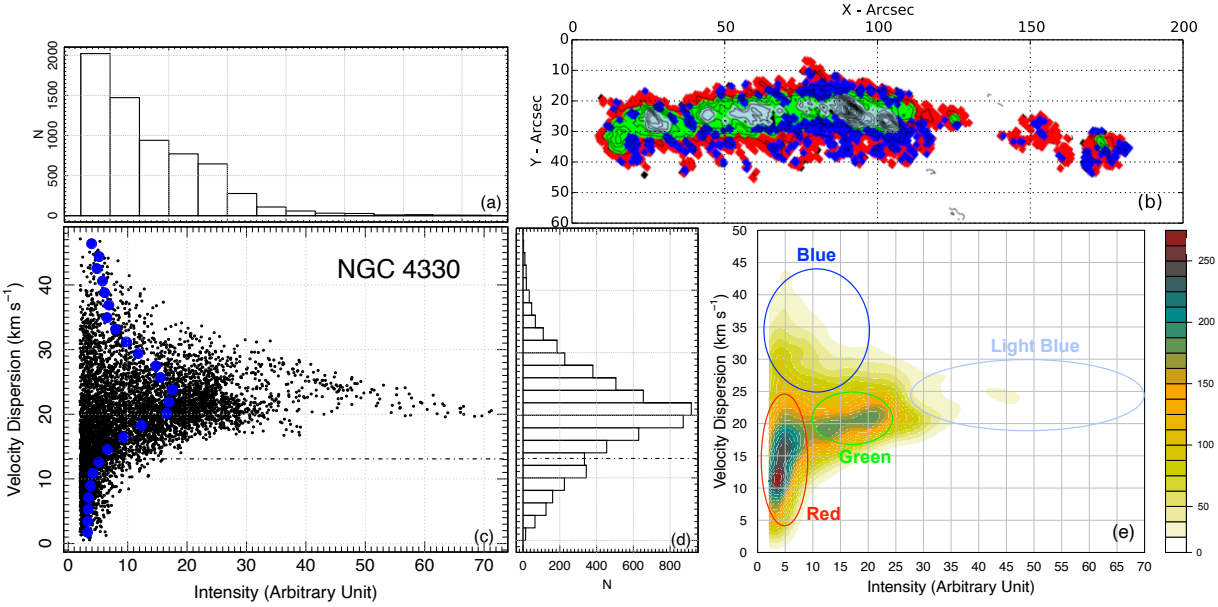

Fig. C.3. GHASP velocity dispersion properties of NGC 4330. Panel (a): Intensity histogram. Panel (b): Loci, in the galaxy, of the different areas shown in panel (e) with different colours (red, green, blue, and light blue), on top of which Hα isocontours have been superimposed. Panel (c): Velocity dispersion versus emission intensity diagnostic diagram. Each black dot represents a pixel, and the blue dots represent the mean of the intensity in each velocity dispersion bin. Panel (d): Velocity dispersion histogram. Panel (e): Pixel density map of the velocity dispersion versus intensity diagram. The colour bar represents pixel density. The dashed line in plots (c) and (d) represents the LSF $\sigma_{\rm LSF}$.

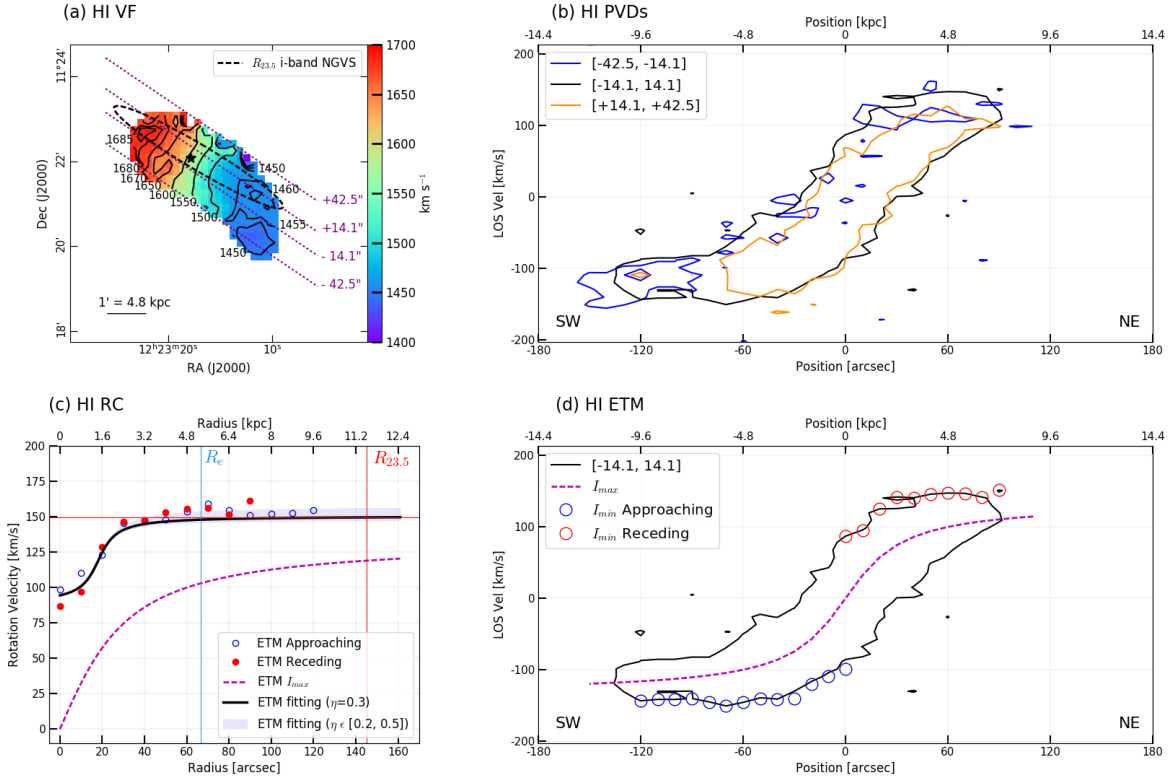

Fig. C.4. HI emission data of NGC 4330 from Chung et al. (2009). Panel (a): Cold gas velocity field on which the positions of pseudo-slits are superimposed (~28 arcsec wide) parallel to the kinematic major axis and the ellipse fitted to the isophote of surface brightness $\mu(i) = 23.5$ mag arcsec^{-2} of the NGVS i-band image, which traces the stellar disc. Panels (b) and (d): Outermost contour of the PVDs. Panel (b) corresponds to the three pseudo-slit positions drawn in panel (a), and panel (d) corresponds to the central pseudo-slit position. The red and blue circles indicate the position of the minimum intensity of the receding and approaching side, respectively, while the dashed line indicates the maximum intensity. Both entities are used to estimate the terminal velocity and to compute the RC using the ETM method. Panel (c): RC computed using the ETM, where the terminal velocity is represented by empty blue circles for the receding side and the filled red circles for the approaching side. The black solid line indicates the best fit to these points using $\eta = 0.3$, the shaded area shows the rotation velocity amplitude for $\eta = [0.2, 0.5]$, the purple dashed line indicates the RC computed from the PVD maximum intensity, and the red and blue vertical lines indicate the photometric and effective radius, respectively.

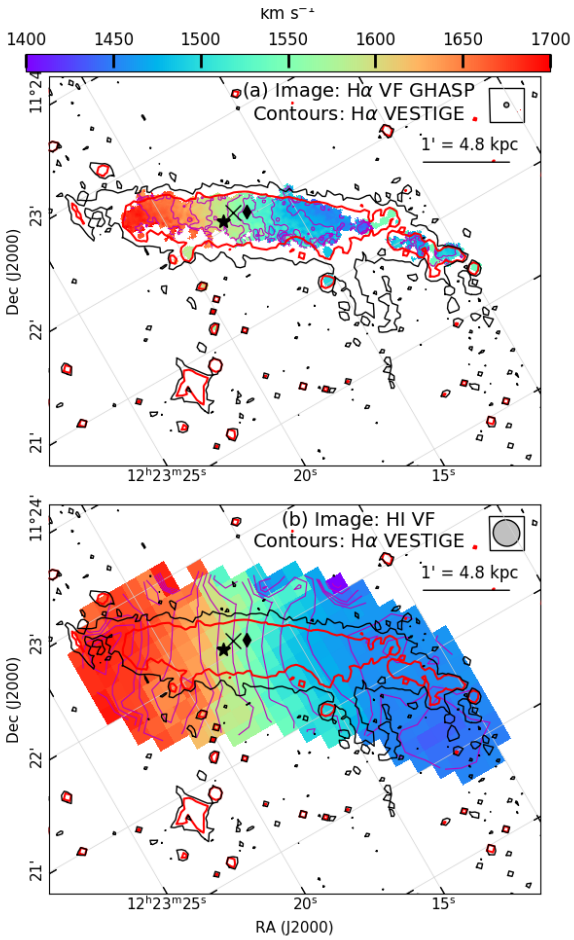

Fig. C.5. Comparison between the GHASP Hα (upper panel) and the HI (lower panel, Chung et al. 2009) velocity fields of NGC 4330. The inner and outer black contours are at $\Sigma(H\alpha) = 3 \times 10^{-18}$ and 1.25×10^{-16} erg s^{-1} cm^{-2} arcsec^{-2}, respectively, and the red contour $\Sigma(H\alpha) = 10^{-17}$ erg s^{-1} cm^{-2} arcsec^{-2}. The black diamond, the cross, and the star indicate the position of the CO, Hα, and HI emission kinematic centres, respectively. To align the maps horizontally, both are rotated i = 59°, the photometric PA of the galaxy. The grey ellipses encapsulated in a box located in the upper-right corner of each panel represent the sizes of the Hα mean seeing disc (upper panel) and of the HI beam (upper panel).

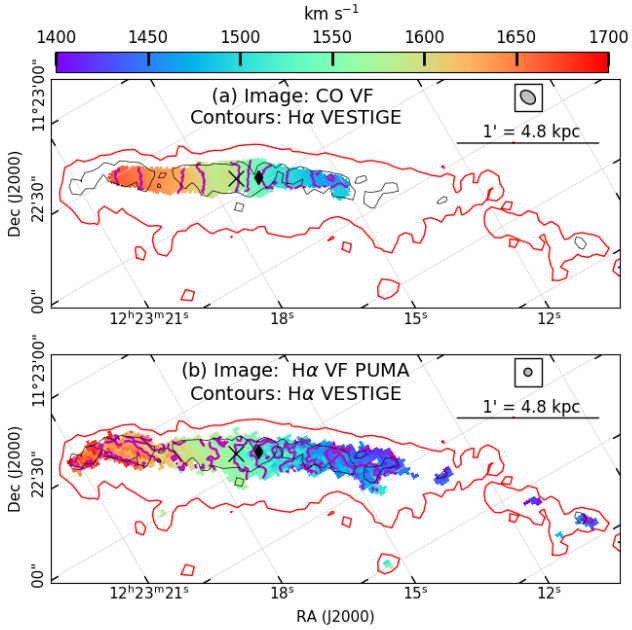

Fig. C.6. Comparison between the ^{12}CO (upper panel; Lee et al. 2017) and the PUMA Hα (lower panel) velocity fields of NGC 4330. The inner black contours and the red outer contours are at $\Sigma(H\alpha) = 10^{-17}$ and $1.25{\times}10^{-16}$ erg s^{-1} cm^{-2} arcsec^{-2}, respectively. The black diamond and the cross indicate the position of the CO and Hα emission kinematic centres, respectively. To align the maps horizontally, both are rotated i = 59°, the photometric PA of the galaxy. The grey ellipses located in the upper-right corner of each panel represent the sizes of the CO beam (upper panel) and of the Hα mean seeing disc (lower panel).

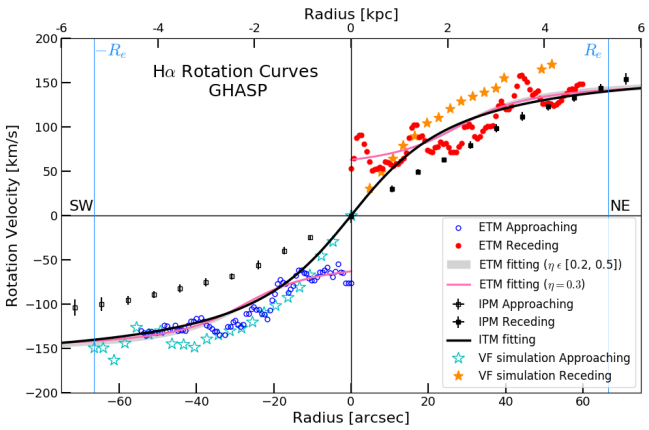

Fig. C.7. Comparison between observed and simulated unfolded RCs. The simulated velocity field shown in panel (c) of Fig. 11 has been used to measure the RC along the major axis of the galaxy; the receding and approaching sides are respectively represented by filled orange and opened cyan stars (⋆) and superimposed onto the GHASP observed and modelled RCs already displayed in panel (c) of Fig. 3, using the same symbols, colours, and lines. The blue vertical lines indicate the position of the effective radius.

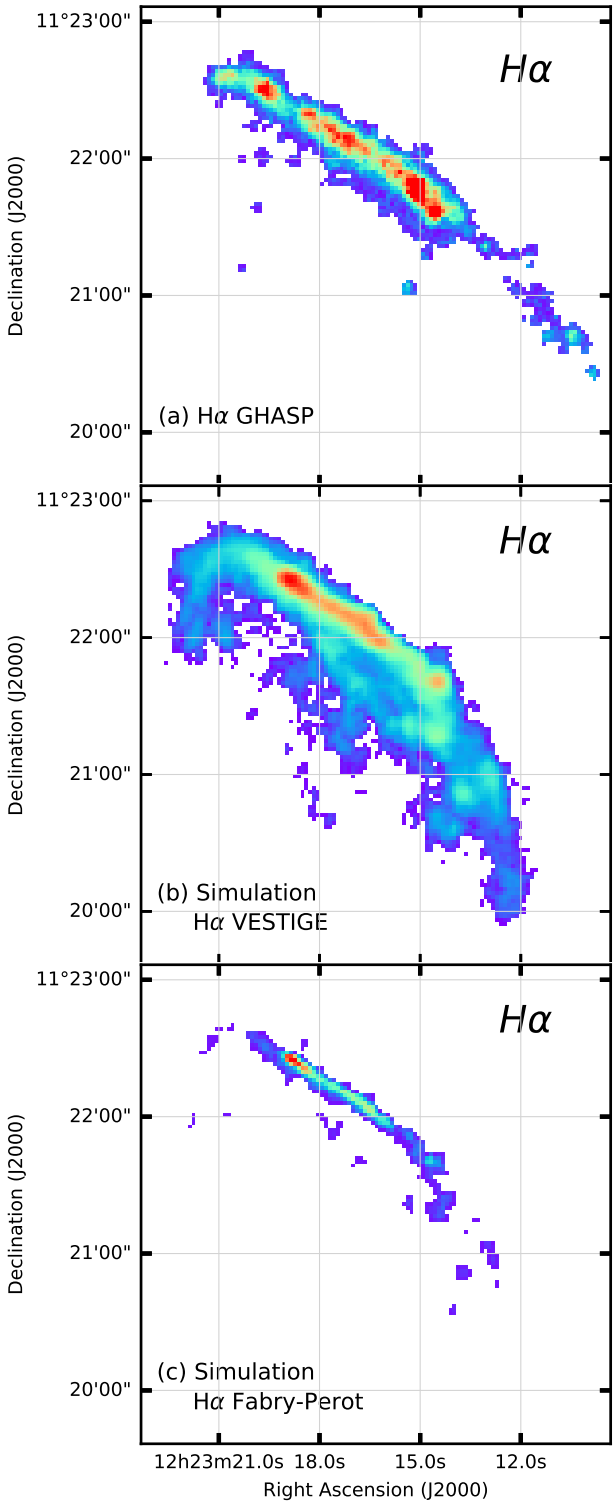

Fig. C.8. GHASP (panel (a)) and simulated Hα surface brightness (panels (b) and (c)) of NGC 4330, with scales identical to those used in Fig. 2 (d), i.e. with a threshold limit $\Sigma(H\alpha) \simeq 10^{-17}$ erg s^{-1} cm^{-2} arcsec^{-2}. The low level cuts used to display the simulated Hα images have been chosen to show the low column density ionised gas reached by the simulations (panel (b)) and at higher surface brightness levels ($\Sigma(H\alpha) \simeq 2{\times}10^{-17}$ erg s^{-1} cm^{-2} arcsec^{-2}; panel (c)), matching the typical surface brightness limit of VESTIGE and FP observations, respectively.